Article

Not peer-reviewed version

High-Performance of Mn_2O_3 Electrodes for Hydrogen Evolution Using Natural Bischofite Salt from Atacama Desert. A Novel Application for Solar Saline Water Splitting

Felipe M. Galleguillos Madrid *, Sebastian Salazar-Avalos, Edward Fuentealba, Susana Leiva-Guajardo, Luis Caceres, Carlos Portillo, Felipe Sepulveda, Ivan Brito, José Ángel Cobos-Murcia, Omar F. Rojas-Moreno, Victor Jimenez, Eduardo Schott, Alvaro Soliz *

Posted Date: 9 August 2024

doi: 10.20944/preprints202408.0640.v1

Keywords: saline water splitting; hydrogen evolution reaction (HER); bischofite; superposition model

Article

High-Performance of Mn_2O_3 Electrodes for Hydrogen Evolution Using Natural Bischofite Salt from Atacama Desert. A Novel Application for Solar Saline Water Splitting

Felipe M. Galleguillos Madrid [1,*], Sebastián Salazar-Avalos [1], Edward Fuentealba [1], Susana Leiva-Guajardo [1], Luis Cáceres [2], Carlos Portillo [1], Felipe Sepúlveda [3], Iván Brito [4], José Ángel Cobos-Murcia [5], Omar F. Rojas-Moreno [6], Víctor Jimenez-Arevalo [7], Eduardo Schott [8] and Alvaro Soliz [9,*]

[1] Centro de Desarrollo Energético Antofagasta, Universidad de Antofagasta, 1240000, Antofagasta, Chile. (F.M.G.M), (S.SA)
[2] Departamento de Ingeniería Química y Procesos de Minerales, Universidad de Antofagasta, Av. Universidad de Antofagasta 02800, Antofagasta 1271155, Chile; luis.caceres@uantof.cl (L.C.)
[3] Departamento de Ingeniería en Minas. Universidad de Antofagasta, 1240000 Antofagasta, Chile. (F.S)
[4] Departamento de Química, Facultad de Ciencias Básicas, Universidad de Antofagasta, Antofagasta, Chile (I.B)
[5] Instituto de Ciencias Básicas e Ingeniería. Universidad Autónoma del Estado de Hidalgo. Carr. Pachuca - Tulancingo km. 4.5, Mineral de la Reforma, Hidalgo, México. C.P. 42184. (J.A.CM)
[6] Faculty of Mechanic, Electronic and Biomedical Engineering, Universidad Antonio Nariño, Tunja 150002, Colombia (O.F.RM)
[7] Departamento de Química de los Materiales, Facultad de Química y Biología, Universidad de Santiago de Chile, Av. Libertador B. O'Higgins 3363, Santiago, Chile; (V.J)
[8] Departamento de Química Inorgánica, Facultad de Química y Farmacia, Centro de Energía UC, Centro de Investigación en Nanotecnología y Materiales Avanzados CIEN-UC, Pontificia Universidad Católica de Chile, Avenida Vicuña Mackenna, 4860, Santiago, Chile. (E.S)
[9] Departamento de Ingeniería en Metalurgia, Universidad de Atacama, Av. Copayapu 485, Copiapó 1530000, Chile (A.S)
* Correspondence: felipe.galleguillos.madrid@uantof.cl

Abstract: Solar saline water splitting is a promising approach for sustainable hydrogen production, harnessing abundant solar energy and the availability of brine resources, especially in the Atacama Desert. Bischofite ($MgCl_2{\cdot}6H_2O$), a naturally occurring salt, has garnered significant attention due to its wide range of industrial applications and the challenges associated with efficient hydrogen production in arid or hyper arid locations. This work discloses the electrochemical performance of Mn_2O_3 electrodes using a superposition model based on mixed potential theory and evaluates the superficial performance of this electrode in contact with a 0.5 M nature Bischofite salt solution focusing on hydrogen evolution reaction (HER), and oxygen reduction reaction (ORR), that occurs during saline water splitting. The application of the non-linear superposition model provides valuable electrochemical kinetic parameters that complement the understanding of Mn_2O_3, this being one of the novelties of the manuscript.

Keywords: saline water splitting; hydrogen evolution reaction (HER); bischofite; superposition model

1. Introduction

The Atacama Desert, have substantial deposits of bischofite mineral ($MgCl_2{\cdot}6H_2O$) in a form of magnesium chloride recovery from solar evaporation process used for lithium recovery. The recovery of bischofite in the Atacama Desert involves mining these subterranean deposits. Bischofite mineral

 doi:10.20944/preprints202408.0640.v1

is notably found in the Atacama Desert. This mineral is present in the well brine located in the altitude places.

The electrochemical stability of electrodes in water splitting process is essential for ensuring the long-term efficiency and effectiveness of HER-based energy systems. Other oxides with different valence states, such as Mn_3O_4 and Mn_2O_3 are also possible cathodic materials candidates. Mn_2O_3 has generated interest because of its high theoretical specific capacity and energy density formed α-Mn_2O_3 between 500 to 800°C [2] and forming ternary oxides as Mn_2O_3 [3–5]. The family of MnO_2 is characterized by a variety of polymorphs with both open (with tunnels) and laminar structures of α-MnO_2 as hollandite, todorokite, and birnessite [6]. Mn_2O_3 powder offers significant advantages in terms of cost-effectiveness and abundance compared to traditional noble metal catalysts, where the use of abundant and affordable materials for HER catalysis is essential for promoting large-scale hydrogen production and making it economically viable. Mn_2O_3 powder presents an opportunity to address the cost and availability concerns associated with noble metal catalysts, thereby accelerating the adoption of hydrogen as a clean and sustainable energy carrier. The interaction between the Mg and Mn powder plays a significant role in the HER activity and selectivity during cathodic subprocess. Understanding the structural aspects of Mn_2O_3 powder and its correlation with catalytic performances is crucial for further optimizing the properties and tailoring it for specific applications. Furthermore, Mn_2O_3 powder demonstrates excellent performance not only in the HER but also in other important electrochemical reactions, such as the oxygen evolution reaction (OER) and oxygen reduction reaction (ORR) [7]. However, currently there is a lack of plausible models that accurately describe the electrochemical and oxidation parameters during the mechanisms. Its versatility and multifunctionality make it a valuable candidate for integration into various renewable energy conversion and storage devices, including water electrolyzes and fuel cells. The ability to perform multiple electrochemical reactions with high efficiency further highlights the potential of Mn_2O_3 powder as a versatile catalyst for clean energy technologies.

This manuscript presents pioneering insights into the utilization of Mn_2O_3 powder as an electrocatalyst for the HER, and ORR mechanisms using natural Bischofite from Atacama Desert. The study aims to provide a comprehensive understanding of the electrochemical behavior exhibited by Mn_2O_3 powder electrodes during direct saline water splitting processes. This is performed in an artificial 0.5 M $MgCl_2$ and 0.5 M of natural Bischofite solutions using a superposition model based on mixed potential theory for recovery an electrochemical and kinetics parameter of HER and ORR mechanisms. Additionally, a comprehensive surface analysis is conducted using scanning electron microscopy (SEM), X-ray diffraction (DRX), and energy-dispersive X-ray spectroscopy (EDS) imaging techniques.

2. Materials and Methods

2.1. Synthesis of Mn_2O_3

The active material Mn_2O_3 was prepared by means of the co-precipitation method, from a solution (que se le agrega) containing $MgSO_4$ (sigma-aldrich, 99% purity), $MnSO_4 \bullet H_2O$ (sigma-aldrich, 99% purity) with a ratio of 1:2 respectively. The solution contains dissolved [1M] NaOH (sigma-aldrich, 99% purity) to keep the alkaline media and distilled water with 18.0 mΩ/cm of resistivity. The solution was kept under magnetic stirring (500 rpm) for 20 h to complete the reaction. The product of this reaction is a pink solid powder, which is subsequently filtered and dried at 80°C for 36 h. This last obtained powder is washed 5 times with plenty of deionized water to eliminate the remaining Na^+ and SO_4^{2-} ions remnants present in the precipitate obtained after the reaction). Once the solid is clean, it is introduced into a furnace at a temperature of 800°C for 6 h to form the Mn_2O_3 material and then allowed to cool to room temperature. The Mg are incorporated into de Mn_2O_3 dispersed over the spinel.

 doi:10.20944/preprints202408.0640.v1

2.2. Electrochemical Measurements of Mn_2O_3 Electrode

The electrochemical measurements procedure was designed to examine the kinetic of the partial electrochemical reactions on the Mn_2O_3 spinel electrode immersed in 0.5 M $MgCl_2$ and 0.5 M of natural Bischofite solutions, focusing the attention on the HER, ORR, and Mn oxidation reaction (MnOR). A modified carbon paste electrode was prepared by mixing 0.2 g of Mn_2O_3 powder, 0.25 g of graphite powder, and 0.2 cm^3 of paraffin wax up to obtain a homogeneous paste. This paste was tightly packed into a plastic Teflon sheath (4 mm in diameter and 10 mm in length) which have with adequate perforations to maintain electrical contact, through a copper wire and the Mn_2O_3 powder, with the rotating disc electrode (RDE) system. Current density vs potential curves were obtained by linear sweep voltammetry (LSV) measurements using a BASI/RDE-2 rotating electrode interphase connected to an Epsilon potentiostat/galvanostat in a conventional 3-electrode cell, in which, the carbon paste electrode with Mn_2O_3 powders acts as working electrode, a platinum wires acts as counter electrode, and an Ag/AgCl (4M KCl Sat.) as a reference electrode (RE). All potentials reported are referred to as the standard hydrogen electrode (SHE). The experimental protocol for polarization data was according to a previous work [8] in a potential range between -1000 to 400 mV/SHE. Before each run the Mn_2O_3 spinel electrode was maintained at -1200 mV/SHE for 30 s.

2.3. Kinetic Analysis

The kinetic analysis was performed by applying non-linear fitting to experimental polarization curves obtained from LVS measurements. The superposition model based on the mixed potential theory was considered according to the methodology described in our previous work concerning mass diffusion, charge transfer, and passivation mechanism controls [9–13]. The following set of kinetic expressions (Eqs. 1–4) is used as part of the non-linear fitting methodology, which considers the total current density (i) as a function of the partial current densities for the ORR (i_{O_2}), and HER (i_{H_2}) and MnOR (i_{Mn}):

$$i = i_{H_2} + i_{O_2} + i_{Mn} \quad (1)$$

$$i_{O_2} = i_{0,O_2}\left(\frac{i_{l,O_2} - i_{O_2}}{i_{l,O_2}}\right)^m \cdot e^{\left(\frac{-2.303\eta_{O_2}}{t_{O_2}}\right)} \quad (2)$$

$$i_{H_2} = i_{0,H_2} \cdot e^{\left(\frac{-2.303\eta_{H_2}}{t_{H_2}}\right)} \quad (3)$$

$$i_{Mn} = i_{0,Mn} \cdot e^{\left(\frac{-2.303\eta_{Mn}}{t_{Mn}}\right)} \quad (4)$$

Where, i_{0,O_2}, i_{0,H_2} and $i_{0,Mn}$ are the exchange current densities for ORR, HER, and MnOR respectively, i_{l,O_2} is the limiting current density for ORR, $\eta_{O_2} = E - E_{eqO_2}$, $\eta_{H_2} = E - E_{eqH_2}$ and $\eta_{Mn} = E - E_{eqMn}$ are the overpotentials for ORR, HER, and MnOR respectively, E is the electrochemical potential, E_{eqO_2}, E_{eqH_2} and E_{eqMn} are the equilibrium potentials for ORR, HER, and MnOR, respectively, t_{O_2}, t_{H_2} and t_{Mn} are Tafel slopes for ORR, HER, and MnOR respectively, and m is the kinetic order for the ORR is equal to 1. The kinetic parameters were calculated from the fitting of Eqs. 1-4 to the experimental data.

2.4. Mn_2O_3 Electrode Surface Characterization

The morphological characterization of the samples was performed by energy dispersive X-ray spectroscopy (EDS) using the following instruments, a Zeiss EVO MA 10 (Zeiss, Oberkochen, Germany), and SEM Hitachi model SU-5000 (Tokyo, Japan). The products layer was studied by X-ray diffraction (XRD) in a Shimadzu XRD-600 diffractometer (Shimadzu Corp., Kyoto, Japan) using Cu Kα radiation at an angular step of 0.02° (2θ) and counting time per step of 4s.

3. Results

Figure 1 show a sequence of scanning electron microscopy (SEM) images portraying the synthesized Mn_2O_3 material. These images were captured at varying magnifications: 3000x, 20,000x, and 70,000x. Accompanying these images is the EDS spectrum extracted from the sample. These

 doi:10.20944/preprints202408.0640.v1

micrographs offer a comprehensive view of the material's morphology and structure, highlighting the characteristics of the granules present within the sample. Notably, the Mn_2O_3 granules exhibit a self-limiting growth pattern. The uniformity in their size is readily apparent; the average kernel size is determined to be 598, with a standard deviation of approximately 334.33. While this standard deviation signifies the presence of granules spanning diverse sizes, it is evident that most of these granules tend to cluster around the mentioned average size.

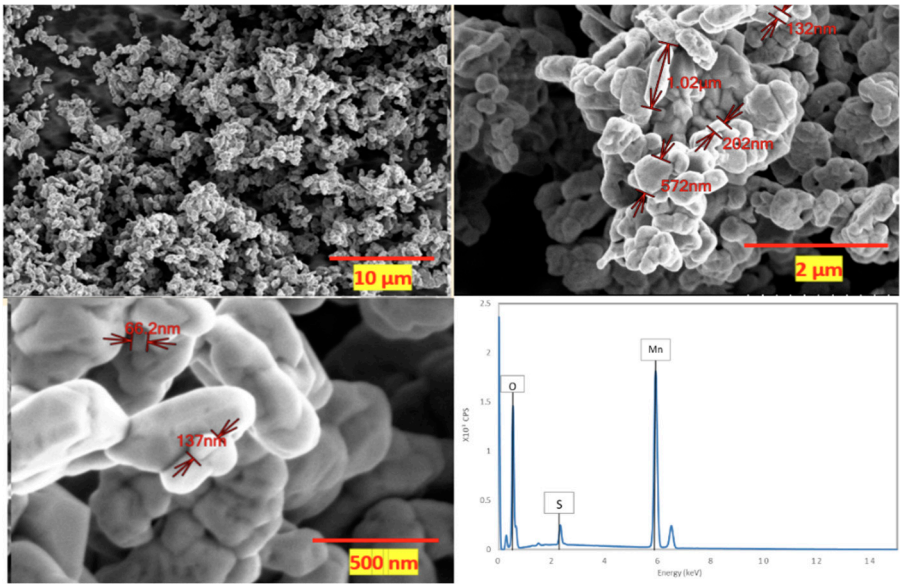

Figure 1. illustrates SEM images depicting the synthesized Mn_2O_3 material, captured at varying magnifications: a) 3,000x, b) 20,000x, and c) 70,000x. Additionally, d) presents the corresponding EDS spectrum obtained from the sample.

Moreover, the EDS spectrum, acquired utilizing secondary electrons at an energy of 30 keV, furnishes an intricate depiction of the elemental constitution of the material. The EDS analysis revealed a composition of 57.53±2.7% manganese (Mn), 31.29±10.36% oxygen (O), and 2.1±4.82% sulfur (S) within the material. Considering the anticipated composition of Mn_2O_3, we would anticipate a manganese (Mn) weight percentage of 69.6% and an oxygen (O) weight percentage of 30.4%. When contrasting these anticipated values with our EDS findings, deviations become evident. The EDS assessment showed a manganese (Mn) proportion of 57.53±2.7%, slightly lower than the projected theoretical value. Correspondingly, the oxygen (O) content measured at 31.29±10.36% is marginally higher, yet this discrepancy falls within the range accounted for by the standard deviation, relative to the theoretical estimate. Numerous factors might contribute to this disparity, ranging from the inherent nature of the synthesis process, which could yield a non-pure Mn_2O_3 product, to potential anomalies or interferences encountered during the EDS analysis. These values underscore that while the sample predominantly comprises manganese (Mn) and oxygen, aligning with the Mn_2O_3 expectation, the presence of sulphur, although in a diminished ratio, raises the prospect of a potential impurity originating from the raw materials employed in the synthesis process. This insight leads to the inference that the synthesis of Mn_2O_3 has been achieved with a noteworthy level of purity.

The results derivative from X-ray diffraction (XRD) analysis of the Mn_2O_3 powder are shown in Figure 2a. Particularly, a discrete peak is distinguished at the 2θ angle of 32.954°, positioning with a crystalline plane of (h, k, l) = 2, 2, 2 and displaying a relative intensity of 100%. This prominent peak assists as a definitive marker for the distinctive crystalline arrangement of Mn_2O_3. By XRD analysis, pivotal visions into the crystalline structure of Mn_2O_3 come to light. At the same time, the results obtained from XRD analysis of the nature bischofite ($MgCl_2{\cdot}6H_2O$) salt are presented in Figure 2b dissimilar peak appears at the 2θ angle closed to 16,32° , corresponding to the crystalline plane with

 doi:10.20944/preprints202408.0640.v1

indices (h, k, l) = 0, 0, 1 and showing a relative intensity of 100%. This peak serves as a clear indicator of the unique crystalline structure of bischofite. The XRD analysis reveals crucial details about the crystalline arrangement of bischofite.

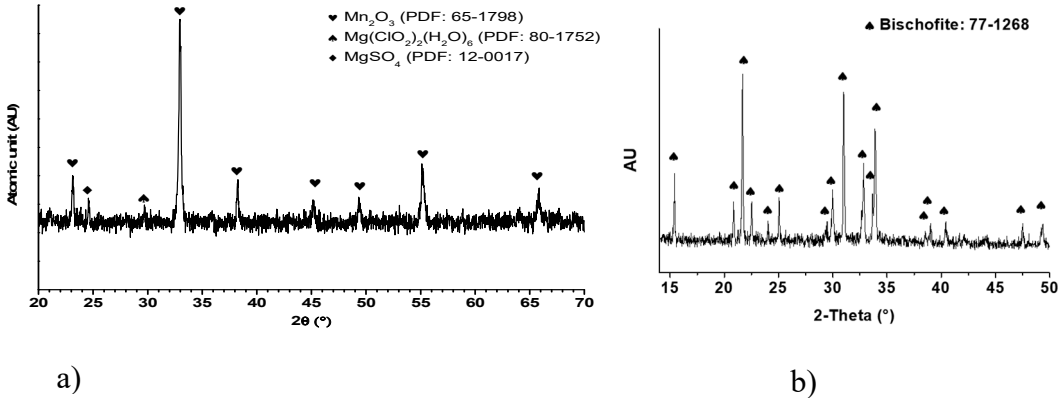

Figure 2. a). XRD pattern of Mn_2O_3 powder, showing a characteristic peak at (h, k, l) = 2, 2, 2 with a 2θ angle of 32.954°, and b) XRD pattern of bischofiter, showing a characteristic peak at (h, k, l) = 2, 2, 2 with a 2θ angle of 16.32°.

The inclusion of Mn^{3+} within the Mn_2O_3 structure introduces specific structural distortions that stem from the Jahn-Teller effect. This effect, inherent to certain cations with distinct electronic configurations, can induce asymmetries within the crystalline arrangement. In the context of Mn_2O_3, these distortions hold the potential to exert an influence over the material's physical and chemical attributes. Mn_2O_3 exhibits a propensity for thermal transformations. Notably, under temperatures nearing 550°C, noteworthy alterations in the tetragonal distortion of the spinel structure can arise. This phenomenon is closely intertwined with the Jahn-Teller effect and the concurrent presence of Mn^{3+} within the structure, signifying a connection between electronic interactions and structural changes.

Through meticulous analysis and comprehensive deliberation of the scanning electron microscopy (SEM) and X-ray diffraction (XRD) findings, unequivocal validation of the successful Mn_2O_3 formation via the employed synthesis process has been attained. The SEM images, in conjunction with the granule morphology characterization and the illustration of their self-limiting growth, furnish compelling substantiation of the synthesized Mn_2O_3 inherent nature and purity. Concurrently, the discernible XRD pattern, showcasing distinctive peaks emblematic of the crystalline Mn_2O_3 structure, reasserts the compound's presence and precise crystalline configuration.

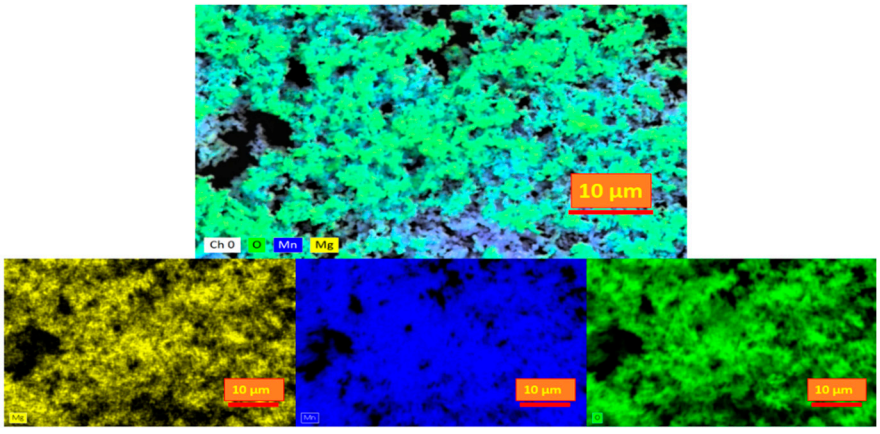

Figure 3. Elemental mapping by EDS analysis for Mn_2O_3 powder.

 doi:10.20944/preprints202408.0640.v1

The confluence of these analytical techniques fortifies the confidence in the acquired outcomes, affirming the unequivocal attainment of Mn_2O_3 formation throughout the synthesis effort. This assurance assumes paramount significance, as the purity and accurate formation of Mn_2O_3 wield direct influence over its properties and potential applications within both research and industrial contexts.

The kinetic study was accomplished by applying non-linear fitting to experimental polarization data, considering the superposition model and mixed potential theory according to the methodology described in our previous works in terms of charge transfer, mass diffusion, and passivation mechanism controls [8,14–17]. Figure 4 provides important information about the electrochemical–kinetic performance of Mn_2O_3 powder during the sub cathodic process in contact with a 0.5 M $MgCl_2$ and 0.5M of Bischofite solutions. Figure 4a displays the linear sweep voltammetry (LSV) results, where the potential window applied during the experiments ranged from -1000 to 400 mV/SHE.

When comparing the performance of Mn_2O_3, where H_2 evolution is predominant, using bischofite solutions shows a slightly higher variation compared to using pure $MgCl_2$ solution during the HER mechanism. This could be due to the presence of natural impurities in the bischofite that might act as co-factors promoting the charge transfer process. As for the cathodic potential range where the hydrogen evolution reaction (HER) mechanism occurs, in the range of -1200 to -1000 mV the Tafel slope (t_{H_2}) were about -471 and -68 mV/dec for pure $MgCl_2$ and nature bischofite, respectively.

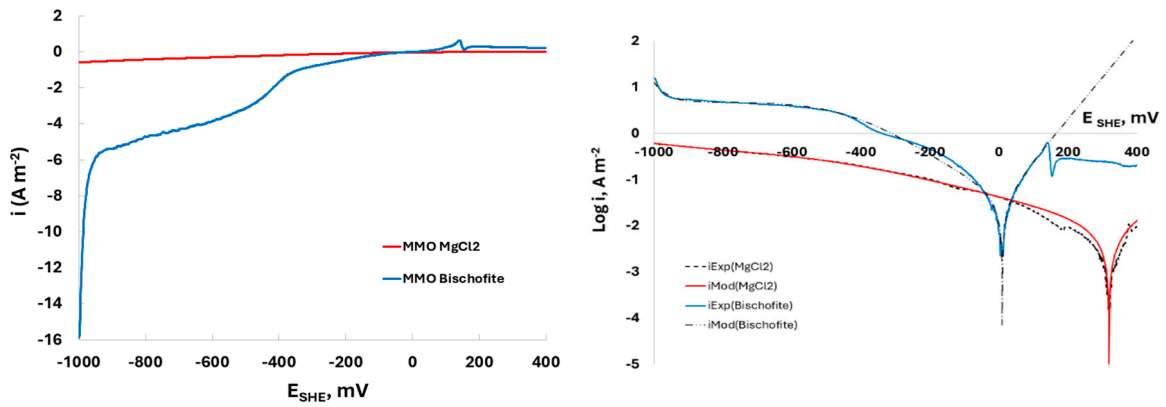

Figure 4. Electrochemical performance of Mn_2O_3 electrode. (a) Linear polarization curves, (b) Tafel polarization curves and superposition model output curves for Mn_2O_3 electrode in aerated 0.5 M $MgCl_2$ and 0.5 M Bischofite, 2 mV/s, and 600 RPM, considering a kinetic order equal to 1.

4. Discussion

A higher Tafel slope suggests slower kinetics and lower efficiency for the HER mechanism. This is observed when using pure $MgCl_2$ as the electrolyte in contact with the Mn_2O_3 electrode, where achieving a higher current density requires a significantly larger increase in overpotential, indicating less effective charge transfer processes. In contrast, when using natural bischofite as the electrolyte, the lower Tafel slope indicates faster kinetics and higher efficiency for the HER mechanism. The smaller increase in overpotential required for higher current densities suggests more effective charge transfer processes and better catalytic performance in the HER range. Higher slope observed for natural bischofite solution indicates that is a more efficient medium for the HER compared to pure $MgCl_2$ electrolyte, due to the presence of natural impurities in bischofite that enhance the catalytic activity of the Mn_2O_3 electrode.

During ORR, the i_{l,O_2} were -0.351 and -4.810 A/m² for pure $MgCl_2$ and nature bischofite, respectively. For nature bischofite, the higher value of i_{l,O_2} indicates limitations in the mass transport, suggesting better performance in facilitating the oxygen-related process. The i_{0,O_2} for both electrolytes were negligible that implies the intrinsic rate of the oxygen-related electrochemical

 doi:10.20944/preprints202408.0640.v1

reaction is too much low in both cases. These low i_{0,O_2} recommends that the kinetics are slow at equilibrium [18–20].

The resistance of Mn_2O_3 powder electrode in contact with pure $MgCl_2$ and nature Bischofite solutions reveals values of E_{corr} and i_{corr} equals 324 and 9 mV/SHE and $5.66 \cdot 10^{-3}$ and $3.89 \cdot 10^{-2}$ A/m², respectively. The E_{corr} and i_{corr} values indicate a high resistance of corrosion during HER mechanims, which is supported by the performance of the Evans curve shown in Figure 4b and the electrochemical kinetic parameters for HER, ORR, and MnOR, tabulated in Table 1.

Table 1, presents the key corrosion and kinetic parameters obtained from the application of the superposition model, utilizing Equations 1 to 4. The parameters are presented in relation to their respective controls, including charge transfer, mass diffusion, and dissolution mechanisms. This comprehensive analysis provides valuable insights into the governing factors and mechanisms influencing the corrosion behaviour in the studied system.

Table 1. Kinetic and corrosion parameters calculated from experimental polarization curves for $MgMn_2O_3$ steel immersed in $MgCl_2$ solutions considering an order 0.5.

Parameters	0.5 M $MgCl_2$	0.5 M Bischofite
i_{0,H_2}, A/m²	$-1.40 \cdot 10^{-2}$	$-9.85 \cdot 10^{-9}$
t_{H_2}, mV/dec.	-471	-68
i_{0,O_2}, A/m²	$-3.12 \cdot 10^{-4}$	$-5.78 \cdot 10^{-6}$
t_{O_2}, mV/dec.	-400	-213
i_{l,O_2}, A/m²	-0.351	-4.810
$i_{0,Mn}$, A/m²	$2.61 \cdot 10^{-8}$	$3.45 \cdot 10^{-6}$
t_{Mn}, mV/dec.	143	111
E_{corr}, mV/SHE	324	9
i_{corr}, A/m²	$5.66 \cdot 10^{-3}$	$3.89 \cdot 10^{-2}$

The Tafel slope for HER using Mn_2O_3 in bischofite solutions is -68 mV/dec, indicates that exist a stronger linear relationship between the logarithm of the current density and the overpotential, with a negative slope representing a decrease in overpotential as the current density increases. For other way, the Tafel slope for $MgCl_2$ solutions is -472 mV/dec suggests efficient HER kinetics.

Numerous electrode materials have shown promise for HER mechanims in seawater or brine, it is important to note that the H_2 Tafel slope, represents the rate of the HER, and depend on specific experimental conditions and electrode preparation methods [25,26]. In seawater the Pt is often considered the standard for HER due to its excellent catalytic activity with Tafel slope typically ranges from around -30 to -40 mV/dec [27]. The Tafel slope of Ni-Fe alloys fluctuate from -91 to -149 mV/dec and depending on the specific Ni-Fe alloy composition and the surface modifications [28]. On the other way, Ni-Mo has Tafel slopes in a range from -40 to -60 mV/dec. The Tafel slope for CoP material is typically between -40 to -50 mV/dec in 1 M KOH [29–31].

5. Conclusions

The use of Mn_2O_3 powder as electrodes for hydrogen evolution reactions (HER) in contact with solutions of pure $MgCl_2$ and natural bischofite salt shows significant differences in electrochemical performance and kinetic parameters. The kinetic analysis using non-linear fitting proved efficient. This superposition model, based on mixed potential theory, effectively described the controls of mass diffusion, charge transfer, and oxidation mechanisms during saline water splitting. The Tafel slopes from Evans curves indicate that natural bischofite salt is more efficient for the HER mechanism, with a Tafel slope of -68 mV/dec compared to -471 mV/dec for pure $MgCl_2$. This lower Tafel slope for natural bischofite suggests faster kinetics and higher efficiency, requiring a smaller increase in overpotential to achieve higher current densities, indicating more effective charge transfer processes and better catalytic performance. The limiting current densities (i_{l,O_2}) for the electrolytes were -0.351

 doi:10.20944/preprints202408.0640.v1

A/m² for pure $MgCl_2$ and -4.810 A/m² for natural bischofite salt from the Atacama Desert. The significant increase in the absolute value of the limiting current density for bischofite shows its superior performance in supporting faster oxygen-related processes before mass transport limitations occur. However, the negligible exchange current densities (i_{0,O_2}) for both electrolytes indicate slow intrinsic reaction kinetics at equilibrium, highlighting a common limitation in both systems. Natural bischofite is a superior electrolyte for HER due to its lower Tafel slope and higher limiting current density for oxygen-related processes, suggesting enhanced efficiency and catalytic performance compared to pure $MgCl_2$. These findings demonstrate that bischofite can be an effective and efficient medium for electrochemical applications, particularly in hydrogen evolution and potentially other related electrochemical processes.

Author Contributions: The following statements should be used "Conceptualization, F.M.G.M, S.SA, and A.S.; methodology, F.M.G.M, S.SA, C.P, L.C., and A.S.; software, F.M.G.M, S.SA, L.C., A.S.; validation, F.M.G.M, S.SA. and L.C.; formal analysis, F.M.G.M, S.SA, S.LG, L.C., A.S, F.S, I.B, J.A.CM, O.F.RM, V. and E.S, .; investigation, F.S, I.B, J.A.CM, S. LG, O.F.RM, V.J, and E.S.; resources, F.M.G.M, S.SA, and L.C.,.; data curation, S.SA F.S, I.B, J.A.CM, O.F.RM, V.J, and E.S,.; writing—original draft preparation, F.M.G.M, S.SA, L.C., A.S, S.SA F.S, I.B, J.A.CM, O.F.RM, V.J, and E.S,.; writing—review and editing, F.M.G.M, S.SA, L.C., A.S, S.SA F.S, I.B, J.A.CM, O.F.RM, V.J, and E.S, .; visualization, F.M.G.M, and S.SA.; supervision, F.M.G.M.; project administration, F.M.G.M.; funding acquisition, F.M.G.M.

Funding: Please add: This research received no external funding.

Acknowledgments: The authors acknowledge the support of ANID through research grant FONDECYT N° 11230550, and the Project DIUDA N° 22430 from the Universidad de Atacama. The authors would like to thank the Programa de Doctorado en Energía Solar of the Universidad de Antofagasta, Chile and ANID/ FONDAP 1522A0006 Solar Energy Research Center SERC-Chile.

Conflicts of Interest: The authors declare no conflicts of interest.

References

1. D. Eberhardt, E. Santos, and W. Schmickler, "Hydrogen evolution on silver single crystal electrodes — first results 1," vol. 461, pp. 76–79, 1999.
2. W. Wei, X. Cui, W. Chen, and D. G. Ivey, "Manganese oxide-based materials as electrochemical supercapacitor electrodes," Chem Soc Rev, vol. 40, no. 3, pp. 1697–1721, Feb. 2011, doi: 10.1039/c0cs00127a.
3. N. N. Sinha and N. Munichandraiah, "Electrochemical conversion of $LiMn_2O_4$ to $MgMn_2O_4$ in aqueous electrolytes," Electrochemical and Solid-State Letters, vol. 11, no. 11, pp. 3–6, 2008, doi: 10.1149/1.2972990.
4. C. Ling and F. Mizuno, "Phase stability of post-spinel compound AMn2O4 (A = Li, Na, or Mg) and its application as a rechargeable battery cathode," Chemistry of Materials, vol. 25, no. 15, pp. 3062–3071, 2013, doi: 10.1021/cm401250c.
5. M. F. Rahman and D. Gerosa, "Preparation of Cathode Material for Rechargeable Magnesium Battery Application," in Global Engineering, Science and Technology Conference, 2015, pp. 2–6.
6. C. Miralles and R. Gómez, "Proving insertion of Mg in Mn2O3 electrodes through a spectroelectrochemical study," Electrochem commun, vol. 106, Sep. 2019, doi: 10.1016/j.elecom.2019.106512.
7. J. H. Mokkath, M. Jahan, M. Tanaka, S. Tominaka, and J. Henzie, "Temperature-dependent electronic structure of bixbyite α-Mn2O3 and the importance of a subtle structural change on oxygen electrocatalysis," Sci Technol Adv Mater, vol. 22, no. 1, pp. 141–149, 2021, doi: 10.1080/14686996.2020.1868949.
8. L. Cáceres, Y. Frez, F. Galleguillos, A. Soliz, B. Gómez-silva, and J. Borquez, "Aqueous dried extract of skytanthus acutus meyen as corrosion inhibitor of carbon steel in neutral chloride solutions," Metals (Basel), vol. 11, no. 12, 2021, doi: 10.3390/met11121992.
9. L. Cáceres, L. Herrera, and T. Vargas, "Corrosion kinetics studies of AISI 1020 carbon steel from dissolved oxygen consumption measurements in aqueous sodium chloride solutions," Corrosion, vol. 63, no. 8, pp. 722–730, 2007, doi: 10.5006/1.3278421.
10. L. Cáceres, T. Vargas, and M. Parra, "Study of the variational patterns for corrosion kinetics of carbon steel as a function of dissolved oxygen and NaCl concentration," Electrochim Acta, vol. 54, no. 28, pp. 7435–7443, 2009, doi: 10.1016/j.electacta.2009.07.078.
11. L. Cáceres, T. Vargas, and L. Herrera, "Influence of pitting and iron oxide formation during corrosion of carbon steel in unbuffered NaCl solutions," Corros Sci, vol. 51, no. 5, pp. 971–978, 2009, doi: 10.1016/j.corsci.2009.02.021.

 doi:10.20944/preprints202408.0640.v1

12. L. Cáceres, T. Vargas, and L. Herrera, "Determination of electrochemical parameters and corrosion rate for carbon steel in un-buffered sodium chloride solutions using a superposition model," Corros Sci, vol. 49, no. 8, pp. 3168–3184, 2007, doi: 10.1016/j.corsci.2007.03.003.
13. C. Luis, Y. Frez, F. Galleguillos, A. Soliz, G. Benito, and J. Borquez, "Aqueous Dried Extract of Skytanthus acutus Meyen as Corrosion Inhibitor of Carbon Steel in Neutral Chloride Solutions," Metals (Basel), vol. 11, no. 12, pp. 1–23, 2021, doi: 10.3390/met11121992.
14. L. Cáceres, T. Vargas, and M. Parra, "Study of the variational patterns for corrosion kinetics of carbon steel as a function of dissolved oxygen and NaCl concentration," Electrochim Acta, vol. 54, no. 28, pp. 7435–7443, 2009, doi: 10.1016/j.electacta.2009.07.078.
15. L. Cáceres, T. Vargas, and L. Herrera, "Influence of pitting and iron oxide formation during corrosion of carbon steel in unbuffered NaCl solutions," Corros Sci, vol. 51, no. 5, pp. 971–978, 2009, doi: 10.1016/j.corsci.2009.02.021.
16. A. Soliz and L. Cáceres, "Corrosion behavior of carbon steel in LiBr in comparison to NaCl solutions under controlled hydrodynamic conditions," Int J Electrochem Sci, vol. 10, no. 7, pp. 5673–5693, 2015.
17. A. Soliz, D. Guzmán, L. Cáceres, and F. M. G. Madrid, "Electrochemical Kinetic Analysis of Carbon Steel Powders Produced by High-Energy Ball Milling," Metals (Basel), vol. 12, no. 4, 2022, doi: 10.3390/met12040665.
18. S. Cao et al. $Mn_2O_3$8, no. 9, pp. 6040–6050, Mar. 2016, doi: 10.1021/acsami.5b11955.
19. J. H. Mokkath, M. Jahan, M. Tanaka, S. Tominaka, and J. Henzie, "Temperature-dependent electronic structure of bixbyite α-Mn2O3 and the importance of a subtle structural change on oxygen electrocatalysis," Sci Technol Adv Mater, vol. 22, no. 1, pp. 141–149, 2021, doi: 10.1080/14686996.2020.1868949.
20. M. Jahan, S. Tominaka, and J. Henzie, "Phase pure α-Mn_2O_3 prisms and their bifunctional electrocatalytic activity in oxygen evolution and reduction reactions," Dalton Transactions, vol. 45, no. 46, pp. 18494–18501, 2016, doi: 10.1039/c6dt03158g.
21. K. V. Rybalka, L. A. Beketaeva, N. G. Bukhan'ko, and A. D. Davydov, "Dependence of corrosion current on the composition of titanium-nickel alloy in NaCl solution," Russian Journal of Electrochemistry, vol. 50, no. 12, pp. 1149–1156, 2014, doi: 10.1134/S1023193514120076.
22. F. Cheng, J. Shen, W. Ji, Z. Tao, and J. Chen, "Selective synthesis of manganese oxide nanostructures for electrocatalytic oxygen reduction," ACS Appl Mater Interfaces, vol. 1, no. 2, pp. 460–466, Feb. 2009, doi: 10.1021/am800131v.
23. I. Roche, E. Chaînet, M. Chatenet, and J. Vondrák, "Carbon-supported manganese oxide nanoparticles as electrocatalysts for the Oxygen Reduction Reaction (ORR) in alkaline medium: Physical characterizations and ORR mechanism," Journal of Physical Chemistry C, vol. 111, no. 3, pp. 1434–1443, Jan. 2007, doi: 10.1021/jp0647986.
24. W. Wang, J. Geng, L. Kuai, M. Li, and B. Geng, "Porous Mn_2O_3: A Low-Cost Electrocatalyst for Oxygen Reduction Reaction in Alkaline Media with Comparable Activity to Pt/C," Chemistry - A European Journal, vol. 22, no. 29, pp. 9909–9913, Jul. 2016, doi: 10.1002/chem.201602078.
25. G. E. Badea, I. Maior, A. Cojocaru, and I. Corbu, "The cathodic evolution of hydrogen on nickel in artificial seawater," 2007.
26. T. Shinagawa, A. T. Garcia-Esparza, and K. Takanabe, "Insight on Tafel slopes from a microkinetic analysis of aqueous electrocatalysis for energy conversion," Sci Rep, vol. 5, Sep. 2015, doi: 10.1038/srep13801.
27. L. Xiu et al., "Multilevel Hollow MXene Tailored Low-Pt Catalyst for Efficient Hydrogen Evolution in Full-pH Range and Seawater," Adv Funct Mater, vol. 30, no. 47, Nov. 2020, doi: 10.1002/adfm.201910028.
28. Z. Wang et al., "MnOxFilm-Coated NiFe-LDH Nanosheets on Ni Foam as Selective Oxygen Evolution Electrocatalysts for Alkaline Seawater Oxidation," Inorg Chem, vol. 61, no. 38, pp. 15256–15265, Sep. 2022, doi: 10.1021/acs.inorgchem.2c02579.
29. C. Lyu et al., "Interfacial electronic structure modulation of CoP nanowires with FeP nanosheets for enhanced hydrogen evolution under alkaline water/seawater electrolytes," Appl Catal B, vol. 317, Nov. 2022, doi: 10.1016/j.apcatb.2022.121799.
30. G. Liu et al., "Porous CoP/Co_2P heterostructure for efficient hydrogen evolution and application in magnesium/seawater battery," J Power Sources, vol. 486, Feb. 2021, doi: 10.1016/j.jpowsour.2020.229351.
31. S. Ye et al., "Removing the barrier to water dissociation on single-atom Pt sites decorated with a CoP mesoporous nanosheet array to achieve improved hydrogen evolution," J Mater Chem A Mater, vol. 8, no. 22, pp. 11246–11254, Jun. 2020, doi: 10.1039/d0ta02936j.